Solid State Ionics 300 (2017) 140–148

Contents lists available at ScienceDirect

Solid State Ionics

journal homepage: www.elsevier.com/locate/ssi

Effect of Nb^{5+} content on the high temperature properties of the mixed conductors system $La_{1-x}Ba_xCo_{1-y}Nb_yO_{3-\delta}$ with $0.6 \le x \le 1.0$ and $0 \le y \le 0.4$

C. Setevich [a,b,*], L. Toscani [c], S. Larrondo [c,d], F. Prado [a], A. Caneiro [b]

[a] Departamento de Física, Universidad Nacional del Sur and Instituto de Física del Sur, CONICET, Av. L. N. Alem 1253, 8000 Bahía Blanca, Buenos Aires, Argentina
[b] Centro Atómico Bariloche, Comisión Nacional de Energía Atómica, Av. Bustillo 9500, 8400, S. C. de Bariloche, Rio Negro, Argentina
[c] CINSO-CITEDEF, UNIDEF-CONICET, J.B. de La Salle 4397, 1603 Villa Martelli, Buenos Aires, Argentina
[d] Instituto de Investigación e Ingeniería Ambiental, 3iA – UNSAM, Campus Miguelete, 25 de Mayo y Francia. 1650, San Martín, Buenos Aires, Argentina

ARTICLE INFO

Article history:
Received 12 September 2016
Accepted 2 December 2016
Available online 30 December 2016

Keywords:
Perovskites
Cobaltites
Oxide mixed conductors
Nb-doping
Crystal structure stability
Thermal expansion, impedance spectroscopy

ABSTRACT

The replacement of Co by Nb in the $La_{1-x}Ba_xCo_{1-y}Nb_yO_{3-\delta}$ ($0.6 \le x \le 1.0$) system and its effects on phase stability and high temperature properties of the cubic perovskite phase were investigated by X-ray diffraction, dilatometry, electrical conductivity, oxygen permeation and electrochemical impedance spectroscopy. The incorporation of Nb in the B site stabilizes the cubic perovskite in the as prepared samples. The Nb solubility increases from $y = 0.1$, for the sample with Ba content $x = 0.6$, to $y = 0.4$ for $0.8 \le x \le 1.0$. However, after a heat treatment at 750 °C during 10 days small amounts of secondary phases were detected for samples with $x = 0.9$ and 1.0. The linear expansion of the cubic phases decreases with the Nb content as well as with the Ba content. The minimum value, $\alpha = 12.9 \times 10^{-6}\ K^{-1}$, was obtained for $La_{0.2}Ba_{0.8}Co_{0.6}Nb_{0.4}O_{3-\delta}$. The behavior of electrical conductivity and oxygen permeation data with Nb content is explained from variations in the oxygen vacancy concentration, which is controlled by Nb^{5+} and Ba^{2+} contents. The minimum polarization resistance value, $Rp = 0.08\ \Omega\ cm^2$, was obtained at 600 °C for $La_{0.2}Ba_{0.8}Co_{0.9}Nb_{0.1}O_{3-\delta}$. The low Rp value of this compound and the crystal structure stability of various compositions in the system $La_{1-x}Ba_xCo_{1-y}Nb_yO_{3-\delta}$ with $x \ge 0.7$ and $y \ge 0.1$ make these materials of interest as mixed conductors.

1. Introduction

Oxides with high electronic and ionic conductivities (MIECs) and high catalytic activity for the oxygen reduction reaction (ORR) are intensively studied as IT-SOFC cathode material [1] and oxygen separation membranes [2]. Among different MIEC oxides, many perovskites of general composition ABO_3 with a rare or alkaline earth (Ln, Sr, Ba) in the A site and Co in the B site, exhibit high electronic and oxide ion conductivities values [2–10]. For instance, several compounds of the systems $Ba_{1-x}Sr_xCo_{1-y}Fe_yO_{3-\delta}$ [8,9], $La_{1-x}Sr_xCo_{1-y}Fe_yO_{3-\delta}$ [7] and $La_{1-x}Ba_xCo_{1-y}Fe_yO_{3-\delta}$ [4–6], have shown good performance as IT-SOFCs cathode materials reaching polarization resistance values for the ORR as low as 0.05 Ω cm^2 at 600 °C, in air [5]. In particular, a power density of 1 W/cm^2 at 600 °C was reported using $Ba_{0.5}Sr_{0.5}Co_{0.8}Fe_{0.2}O_{3-\delta}$ (BSCF) as cathode electrode in an anode supported fuel cell [8]. After the synthesis, the crystal structure of BSCF is cubic, however it gradually transforms into a mixture of a cubic perovskite and a hexagonal phase after annealing at $T < 900$ °C in air [11,12], which may be unfavorable for electrochemical applications. A similar behavior was reported for $La_{1-x}Ba_xCoO_{3-\delta}$ (LBCX) compounds with $x \ge 0.6$ [5,6]. One way of stabilizing the cubic perovskite is by means of chemical substitutions [6,13]. Nagai et al. [13] studied many chemical substitutions of Co by cations with higher valence confirming that Fe^{4+} and Nb^{5+} are very effective in stabilizing the cubic perovskite in the $SrCoO_{3-\delta}$ based compounds. Similarly, we have studied the effects of the substitution of Co by Fe on the stability of the cubic perovskite in the $La_{1-x}Ba_xCo_{1-y}Fe_yO_{3-\delta}$ system with $x \ge 0.5$ [6]. As Ba content increases from $x = 0.7$ to 0.9, the Fe content necessary to stabilize the cubic perovskite increases from $y = 0.3$ to 0.6. In this case, the polarization resistance also increases with the Fe content. For BSCF, Fang et al. [14] have reported the suppression of its phase instability at intermediate temperatures (500 °C ≤ T ≤ 800 °C) by means of the substitution of 5 mol% of Nb for (Co,Fe). In the same way, the substitution of Co by Nb and Fe has been used to stabilize the cubic perovskite in the $BaCoO_{3-\delta}$ based compounds leading to

* Corresponding author at: Departamento de Física, Universidad Nacional del Sur and Instituto de Física del Sur, CONICET, Av. L. N. Alem 1253, 8000 Bahía Blanca, Buenos Aires, Argentina.
E-mail address: cristian.martinez.setevich@gmail.com (C. Setevich).

http://dx.doi.org/10.1016/j.ssi.2016.12.016
0167-2738/

$BaCo_{0.7}Fe_{0.2}Nb_{0.1}O_{3-\delta}$ which exhibited improved electrochemical responses [15,16].

Aiming to identify structurally stable oxide mixed conductors and, considering the experimental evidence described above, we have studied the effects of the substitution of Co by Nb on the phase stability and high temperature properties of the $La_{1-x}Ba_xCo_{1-y}Nb_yO_{3-\delta}$ (LBCN) system with $0.6 \le x \le 1.0$ and $0.0 \le y \le 0.4$. Thus, we have determined the phase relationship at temperatures $T \le 900$ °C and studied the effects of the replacement of Co by Nb on the crystal structure, thermal expansion, electrical conductivity, oxygen permeation and polarization resistance as cathode for IT-SOFC by means of electrochemical impedance spectroscopy.

2. Experimental

$La_{1-x}Ba_xCo_{1-y}Nb_yO_{3-\delta}$ samples with $0.6 \le x \le 1.0$ and $0.0 \le y \le 0.4$ and $Ba_{0.5}Sr_{0.5}Co_{0.8}Fe_{0.2}O_{3-\delta}$ (BSCF) were synthesized by a conventional solid-state reaction technique. Required amounts of La_2O_3, previously dried overnight at 1000 °C, in air, $BaCO_3$, $SrCO_3$, Fe_2O_3, Nb_2O_5 and Co_3O_4 were mixed and ground with a mortar and pestle and heat treated at 850 °C for 8 h in air. Subsequently, the powders were ball milled during 15 min using an agate milling media, pressed into pellets and sintered in air at temperatures ranging from 1000 °C to 1300 °C, as detailed in Table 1, during 12 h. Afterwards the samples were cooled at a rate of 5 °C/min to room temperature. X-Ray diffraction (XRD) data were collected at room temperature with a PANanalytical Empyrean diffractometer by using Cu Kα radiation, a graphite monochromator and a 3D PIXEL detector from $2\theta = 10$ to 80° with a counting time of 1 s for each 0.026°. The crystal structures of the samples were analyzed by the Rietveld method using the FullProf Program [17]. High temperature XRD data were collected in the temperature range $20 \le T \le 1000$ °C, under air, using an Anton Paar camera coupled to the PANalytical Empyrean diffractometer.

The linear expansions of the $La_{1-x}Ba_xCo_{1-y}Nb_yO_{3-\delta}$ compounds were measured on rectangular dense samples ($\rho/\rho_{teor} \ge 0.9$) of approximately $8 \times 2.5 \times 1.5$ mm, from room temperature to 1000 °C under flowing air, using a LINSEIS L75PT Series dilatometer. All the samples were heated up to 1000 °C at 5 °C/min, and, after a 1 h dwell, were cooled down to room temperature at a rate of 1 °C/min. They were then once again heated to 1000 °C at a rate of 1 °C/min, in air. Experimental data were corrected using Al_2O_3 as a standard.

High temperature electrical conductivity measurements were carried out in air in the temperature range $25 \le T \le 900$ °C during a heating/cooling cycle at a rate of 1 °C min^{-1} by a standard four-probe DC technique.

Oxygen permeation measurements were performed using an experimental setup that utilizes He as a carrier and a SRI 8610C gas chromatograph. Disk samples of $La_{1-x}Ba_xCo_{1-y}Nb_yO_{3-\delta}$ with density, in most cases, higher than 90% of the theoretical one (see Table 1) were mounted on the top of a supporting alumina tube and sealed with Pyrex glass ring and paste. An alumina ring with the same inner diameter as the Pyrex glass ring was also used as a weight to keep the seal leak-tight while maintaining the same permeation area on both sides of the membrane. While one side of the membrane was open to air ($pO_2 = 0.209$ atm), the other side was exposed to a lower pO_2 value that was controlled by regulating the helium gas flow rate inside the alumina tube. The exiting He gas was sampled by the GC configured with a TCD detector to measure the oxygen and nitrogen partial pressures. Oxygen permeation flux (jO_2) across the membrane was calculated knowing the cross-sectional area of the sample disk, the He gas flow rate, and the oxygen partial pressure in the He carrier gas. It took several hours to obtain the equilibrium oxygen permeation flux at each pO_2 and temperature. Accordingly, the data presented here were collected after reaching the equilibrium jO_2 values. Any nitrogen detected in the carrier gas was used to correct the jO_2 values for air leaks.

Table 1
Temperature of synthesis, T_s, and fraction of the theoretical density ρ/ρ_{teor}, for $La_{1-x}Ba_xCo_{1-y}Nb_yO_{3-\delta}$ pellets used for dilatometry and permeation measurements.

	y = 0.0	y = 0.1	y = 0.2	y = 0.3	y = 0.4
x = 0.6	1100 °C	1150	1200 °C	1300 °C	1300 °C
x = 0.7	1100 °C	1150 °C	Ts = 1200 °C $\rho/\rho_{teor} = 0.93$	1250 °C	1300 °C
x = 0.8	1100 °C 0.86	1150 °C 0.92	1150 °C 0.91	1250 °C 0.90	1250 °C 0.89
x = 0.9	1100 °C	1100 °C	1150 °C 0.93	1200 °C	1200 °C
x = 1.0	1000 °C	1000 °C	1100 °C	1100 °C	1100 °C

The polarization resistance of the LBCN electrodes was studied in air by impedance spectroscopy measurements on electrochemical cells with symmetrical configuration using GDC as electrolyte. Commercial $Ce_{0.9}Gd_{0.1}O_{1.95}$ powder was pressed into 12.5 mm diameter disks, applying a uniaxial pressure of 200 kg/cm^2, and calcined at 1350 °C during 4 h, in air. After sintering, the electrolyte disks were approximately 9.8 mm in diameter and around 0.3 mm thick. The inks for electrode deposition were prepared by mixing the corresponding ceramic powders with ethanol, α-terpineol, polyvinyl butyral, and polyethylene glycol in 40:40:27:2:1 ratio. The electrode configuration consisted of a single layer of LBCN sprayed onto dense GDC electrolyte. After the electrode deposition, the symmetrical cells were heat treated at 950 °C for 1 h, in air. The impedance spectroscopy measurements were performed in the temperature range $450 \le T \le 850$ °C, in static air, by steps of 50 °C. The data acquisition was performed by a potentiostat Autolab PGSTAT-30 fitted with a module FRA2 in a frequency range of $10^{-3} \le f \le 1$ MHz. An AC signal of 20 mV was applied to the cell, under zero DC bias. A very thin platinum ink layer and platinum grids slightly pressed on top of the porous electrodes, were used as current collectors. Impedance diagrams were analyzed using *Z*-view2 software [18]. The microstructure and thickness of the porous layers were characterized by scanning electron microscopy (SEM) using a SEM FEG NovaNano 230 microscope.

3. Results and discussion

3.1. Phase relationship and stability

The phase relationship in the $La_{1-x}Ba_xCo_{1-y}Nb_yO_{3-\delta}$ system with $x \ge 0.6$ and $0.0 \le y \le 0.4$ was studied by X-ray diffraction. XRD patterns were collected after the samples were heat treated at 1000 °C–1250 °C in air for 12 h and cooled down at a rate of 5 °C/min. As the La and Nb contents are raised, the temperature of synthesis (Ts) needed to obtain single phase materials also increases, as detailed in Table 1. For example, for $BaCoO_{3-\delta}$ the synthesis temperature was $T_s = 1000$ °C, which increases to $T_s = 1300$ °C for $La_{0.3}Ba_{0.7}Co_{0.6}Nb_{0.4}O_{3-\delta}$. The $La_{1-x}Ba_xCoO_{3-\delta}$ samples with $x = 0.6$ and 0.7 were found to be single phase, with a cubic perovskite crystal structure, while samples with $x = 0.8$ and 0.9 are a mixture of phases consisting of the cubic perovskite and a hexagonal phase, most likely the 12H, as previously reported [5]. The sample with $x = 1.0$ also resulted single phase but the crystal structure was the 12H hexagonal phase (S.G. $P6_3/mmc$) [6,19]. For Ba contents $x = 0.6$ and 0.7 the replacement of Co by Nb stabilizes the cubic perovskite in the Nb content ranges $0.0 \le y \le 0.1$ and $0.0 \le y \le 0.3$, respectively. For $x = 0.8$ and 0.9, the cubic perovskite was obtained for $0.1 \le y \le 0.4$, while for $x = 1.0$ it was obtained for the Nb range $0.2 \le y \le 0.4$. The formation of the cubic perovskite was verified by XRD. As an example, Fig. 1 shows the XRD patterns of $La_{0.2}Ba_{0.8}Co_{1-y}Nb_yO_{3-\delta}$ with $0.0 \le y \le 0.4$. While the sample with $y = 0$ (Fig. 1a) results in a mixture of phases [5], for $y \ge 0.1$ (Fig. 1b-e) the samples are single phase with the cubic perovskite crystal structure (S.G. *Pm-3m*). Noteworthy, the replacement of 10% of Co by Nb is enough to obtain the cubic perovskite. This behavior was also observed for the samples with $x = 0.9$. The Nb content $y = 0.1$ needed to stabilize

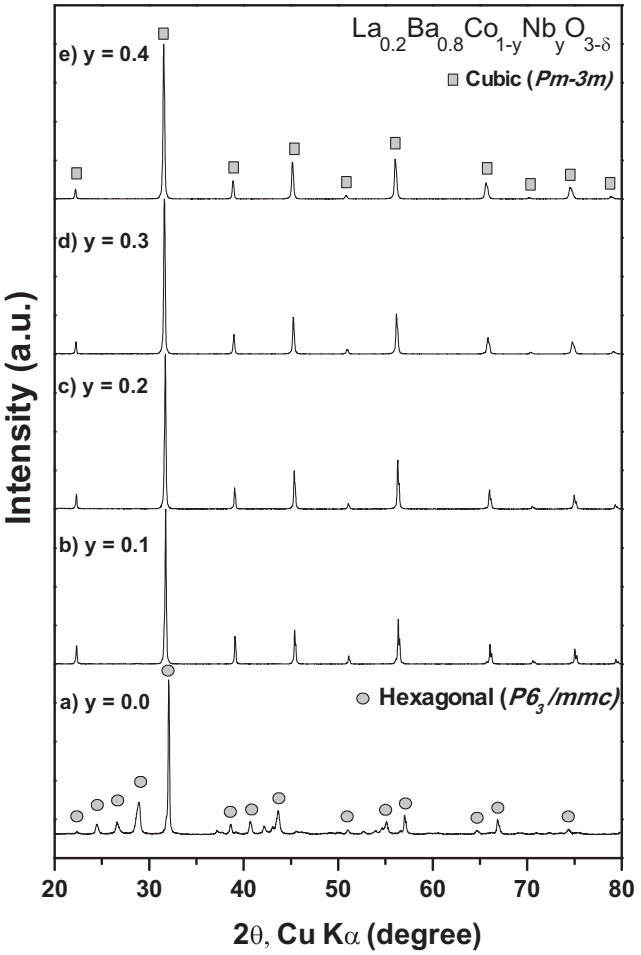

Fig. 1. XRD patterns of $La_{0.2}Ba_{0.8}Co_{1-y}Nb_yO_{3-\delta}$ samples with $0.0 \le y \le 0.4$ heat treated during 12 h between 1100 and 1250 °C, in air.

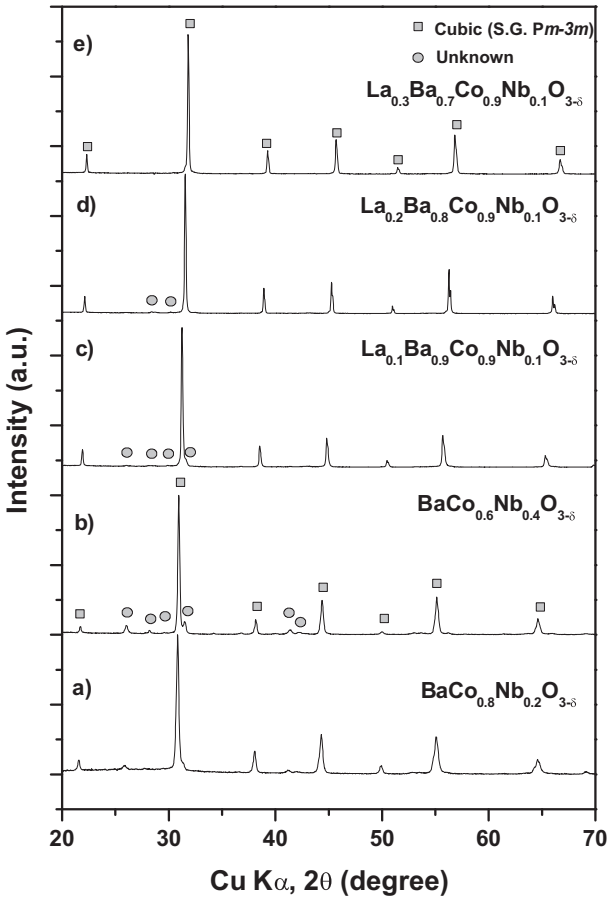

Fig. 2. XRD patterns of $La_{1-x}Ba_xCo_{1-y}Nb_yO_{3-\delta}$ samples heat treated during 10 days at 750 °C, in air: a) $x = 1.0$ and $y = 0.4$; b) $x = 1.0$ and $y = 0.2$; c) $x = 0.9$ and $y = 0.1$; d) $x = 0.8$ and $y = 0.1$; e) $x = 0.7$ and $y = 0.1$.

the cubic phase was found to be lower than the amount of Fe, $y = 0.2$ and 0.3, needed to obtain a similar result for $La_{1-x}Ba_xCo_{1-y}Fe_yO_{3-\delta}$ [6].

The stability of the cubic perovskites containing Nb was tested at $T = 750$ °C, in air, over a period of 10 days. Fig. 2 shows selected XRD patterns after the heat treatment. For $BaCo_{1-y}Nb_yO_{3-\delta}$ with $0.1 \le y \le 0.4$, the XRD data reveal secondary phases, which indicates the cubic phase is unstable at this temperature. For $y = 0.1$ the sample transforms to a mixture of the 2H and 12H hexagonal phases in agreement with data reported by Yamaura et al. [20], while for $0.2 \le y \le 0.4$ the samples transform to a mixture of a cubic and an unknown phase (Fig. 2a and b). Similar behavior was observed for the cubic perovskites with $x = 0.9$, although in this case the secondary phases reflections are barely visible (Fig. 2c). As the Ba content decreases ($x = 0.7$ and 0.8) the intensity of the extra peaks also decreases, with the fraction of secondary phases being very small for $x = 0.8$ and negligible for $x = 0.7$ (Fig. 2d and e). On the other hand, the sample with $x = 0.7$ and Nb content $y = 0.4$ consists of a mixture of cubic perovskites with different compositions. The same happens with those samples with $x = 0.6$ and Nb content $y \ge 0.2$. Fig. 3 resumes the phase relationship for the $La_{1-x}Ba_xCo_{1-y}Nb_yO_{3-\delta}$ system for the as-made samples and those obtained after a heat treatment at 750 °C for 10 days.

Fig. 4 shows the variation of the cubic lattice parameter *a* with the Ba and Nb content. The incorporation of the larger cation Ba^{+2} ($r_{XII} = 1.61$ Å) compared to La^{+3} ($r_{XII} = 1.36$ Å) [21] while Nb content is fixed led to the increase of lattice parameter *a*. On the other hand, the replacement of Co^{+3} ($r_{VI} = 0.61$ Å) and Co^{+4} ($r_{VI} = 0.53$ Å) by the larger cation Nb^{5+} ($r_{VI} = 0.64$ Å) also led to an increment in *a*. The lattice parameters of the cubic phase in the as prepared samples are systematically larger than the values obtained for those samples heat treated at 750 °C. Similar behavior was found for the system $La_{1-x}Ba_xCo_{1-y}Fe_yO_{3-\delta}$ [6].

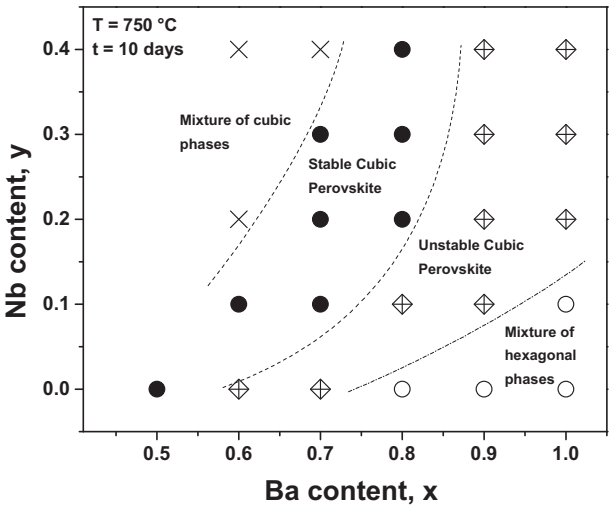

Fig. 3. Scheme of the cubic phase stability as a function of the Ba and Nb content after a heat treatment at 750 °C, during 10 days, in air. ○) Mixture of hexagonal phases, ●) stable cubic perovskite, ⊕) metastable cubic perovskite, x) mixture of cubic phases.

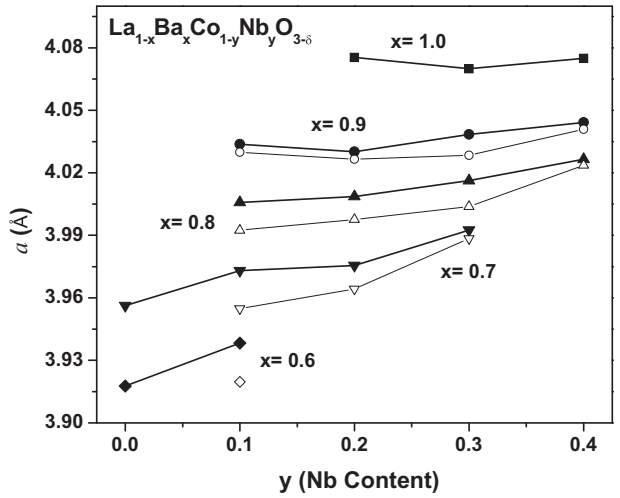

Fig. 4. Variations of the lattice parameter *a*, as a function of the Nb and Ba content for the cubic perovskite phases. Solid symbols correspond to samples cooled at 1 °C/min in air, while open symbols correspond to samples annealed at 750 °C during 10 days.

3.2. Linear expansion measurements

The linear expansion was studied for $La_{1-x}Ba_xCo_{1-y}Nb_yO_{3-\delta}$ in the temperature range 30 °C ≤ *T* ≤ 1000 °C, in air, during cooling/heating runs. Like other cobaltites two effects contribute to the overall expansion of the material: a) the thermal expansion associated with the vibrations of the atoms in the crystal lattice, and b) the chemical expansion related to variations of the oxygen content [22]. Fig. 5a and b show the variation of the relative linear expansion $\frac{\Delta L}{L_0} = \frac{(L-L_0)}{L_0}$ with temperature for $La_{0.2}Ba_{0.8}Co_{1-y}Nb_yO_{3-\delta}$ with 0.0 ≤ y ≤ 0.4. L_0 and L are the initial and actual length during linear expansion measurements, respectively. In the low temperature range *T* ≤ 400 °C, the main contribution is related to the thermal expansion. Above 400 °C the slope of the $\Delta L/L_0$ vs. *T* curves increases indicating the presence of both thermal and chemical contributions to the material expansion [22,23]. Fig. 5a shows the $\Delta L/L_0$ vs. *T* curve for $La_{0.2}Ba_{0.8}CoO_{3-\delta}$. A hysteresis loop is observed in the temperature range 850 °C ≤ *T* ≤ 950 °C. At low temperatures, this sample is a mixture of cubic perovskite and hexagonal phases, being the 12H hexagonal phase the dominant one, as is revealed by XRD data in Fig. 1a. On the other hand, it was reported that a sample of $La_{0.2}Ba_{0.8}CoO_3$ cooled from *T* = 1100 °C to room temperature in a slightly reducing atmosphere, such as argon, results single phase with the cubic perovskite crystal structure [5]. This result indicates that as the oxygen content decreases the crystal structure becomes cubic. Thus, the volume expansion observed during heating at T ~ 950 °C is associated to oxygen loss and reveals the transformation from a mixture of phases to the cubic perovskite. On the other hand, during the cooling process, the volume contraction is related to the incorporation of oxygen atoms by the sample and the phase transformation from the single cubic perovskite phase to a mixture of phases. Fig. 5b shows the $\Delta L/L_0$ vs. *T* curves for $La_{0.2}Ba_{0.8}Co_{1-y}Nb_yO_{3-\delta}$ with Nb content in the range 0.1 ≤ y ≤ 0.4. The stabilization of the cubic phase with y = 0.1 initially causes the growth of the oxygen nonstoichiometry mainly at *T* ≥ 350 °C, that is to say the chemical contribution, but it gradually diminishes as the Nb content increases from y = 0.1 to 0.4 reaching the total linear expansion minimum value of $12.9 \times 10^{-6}\ K^{-1}$ for the sample with y = 0.4 (see Fig. 5b). The variation of the linear expansion coefficient with the Nb content in the temperature range 30 °C ≤ *T* ≤ 900 °C is displayed in the inset of Fig. 5b. Fig. 6, shows the evolution of the $\Delta L/L_0$ vs. *T* curves for $La_{1-x}Ba_xCo_{0.8}Nb_{0.2}O_{3-\delta}$ varying the Ba content in the range 0.7 ≤ x ≤ 1.0 and keeping the Nb content constant at y = 0.2. The chemical contribution to the linear expansion decreases as the Ba content increases and so does the linear expansion coefficient $\alpha = \frac{\Delta L}{\Delta T\ L_0}$, which varies from $17.6 \times 10^{-6}\ K^{-1}$ to $14.6 \times 10^{-6}\ K^{-1}$ as the Ba content changes from x = 0.7 to 1.0 (see the inset in Fig. 6).

On the other hand, the presence of a small hysteresis loop during the cooling/heating runs can be observed in the temperature range 800 °C ≤ *T* ≤ 950 °C in most of the cubic perovskites containing Nb. Contrary to the hysteresis loop observed for $La_{0.2}Ba_{0.8}CoO_{3-\delta}$ (Fig. 5a) for these samples a volume contraction is observed at *T* ≈ 920 °C–950 °C during heating and a volume expansion at *T* ≈ 850–870 °C during cooling. XRD diffraction measurements, in situ, at high temperature, were carried out on a $La_{0.2}Ba_{0.8}Co_{0.6}Nb_{0.4}O_{3-\delta}$ sample. Fig. 7 shows the variation of the lattice parameter of the cubic phase under a heating/cooling process for 700 °C ≤ *T* ≤ 1000 °C. No evidence of a

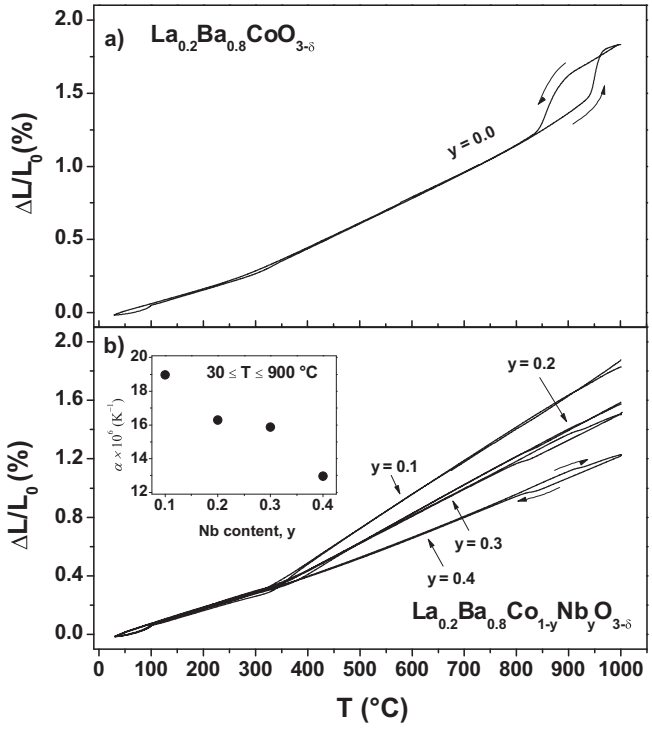

Fig. 5. Relative length change $\Delta L/L_0$ as a function of temperature for $La_{0.2}Ba_{0.8}Co_{1-y}Nb_yO_{3-\delta}$ samples: a) y = 0, b) 0.1 ≤ y ≤ 0.4. The inset in Fig. 5b shows the variation of $\alpha_{30\text{-}900°C}$ as a function of the Nb content.

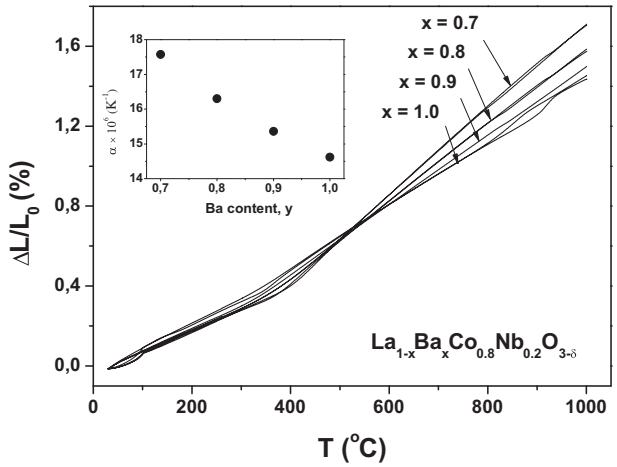

Fig. 6. Relative length change $\Delta L/L_0$ as a function of temperature for $La_{1-x}Ba_xCo_{0.8}Nb_{0.2}O_{3-\delta}$ samples with fixed Nb content y = 0.2 and Ba content 0.7 ≤ x ≤ 1.0. The inset shows the variation of $\alpha_{30\text{-}900°C}$ as a function of the Ba content.

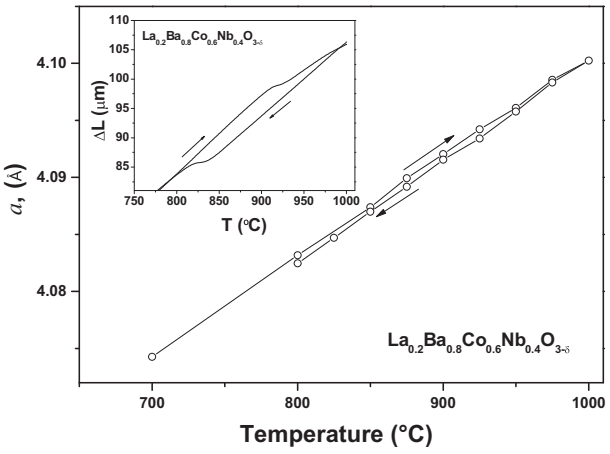

Fig. 7. Variation of the lattice parameter a with temperature of the cubic phase $La_{0.2}Ba_{0.8}Co_{0.6}Nb_{0.4}O_{3-\delta}$. The inset magnify the section of the ΔL vs. T curve where the hysteresis is observed.

structural transformation was detected since the a vs. T curve is smooth and continuous, suggesting the hysteresis could be not related to the cubic phase. In addition, no secondary phases were detected by XRD data in the heating/cooling run that could indicate phase segregation or other processes. Thus, we speculate that the hysteresis could be related to a minority phase hard to detect by XRD.

3.3. Electrical conductivity

Fig. 8 displays the variations of the total electrical conductivity as a function of temperature for the $La_{1-x}Ba_xCo_{1-y}Nb_yO_{3-\delta}$ system. Although these perovskite phases are mixed conductors, the oxide ion conductivity is in general various orders of magnitude smaller than the electronic conductivity [24–26]. Accordingly, the experimental data shown in Fig. 8 correspond, in a good approximation, to the electronic conductivity. Fig. 8a and b display the σ vs. T curves in air for the composition $La_{0.2}Ba_{0.8}Co_{1-y}Nb_yO_{3-\delta}$ with $0 \le y \le 0.4$ and $La_{1-x}Ba_xCo_{0.8}Nb_{0.2}O_{3-\delta}$ with $0.7 \le x \le 1.0$, respectively. In Fig. 8c and d we show the $\ln \sigma T$ *vs.* T^{-1} plots, which for a polaron hopping conduction mechanism [26] would give a linear variation in agreement with the equation,

$$\sigma = \left(\frac{A}{T}\right) \exp\left(-\frac{E_a}{k_B T}\right) \quad (1)$$

where A is a constant, E_a is the hopping activation energy, k_B is the Boltzman constant and T is the absolute temperature. For a given Ba content, σ diminishes when the Nb content increases. For instance, for the $x = 0.8$ samples in the temperature range 600 °C ≤ T ≤ 900 °C, the electrical conductivity varies from ~40 S cm^{-1} to ~10 S cm^{-1} when the Nb content changes from $y = 0.1$ to 0.4 (Fig. 8a). For $La_{0.2}Ba_{0.8}CoO_{3-\delta}$ ($y = 0$), whose majority phase symmetry is hexagonal, the σ values are larger than those obtained for the cubic perovskites. If the Nb content is fixed, σ decreases with the Ba content, as shown in Fig. 8b and d for samples with $y = 0.2$. At low temperatures (20 °C ≤ T < 300 °C), the oxygen content of these samples is assumed constant, thereby σ is thermally activated and the $\log(\sigma T)$ vs. T^{-1} plots should be linear. This behavior was observed for $La_{0.2}Ba_{0.8}Co_{0.6}Nb_{0.4}O_{3-\delta}$ (Fig. 8c) yielding an activation energy $E_a = 0.4$ eV. For samples with $x = 0.8$ and $y \le 0.3$, the $\log(\sigma T)$ vs. T^{-1} curves become nearly parallel, with higher σ values, although the plots are not rigorously linear. This behavior indicates the replacement of Co by Nb reduces the available electronic states leading to larger charge carrier localization, although the activation energy remains close to 0.4 eV. In Fig. 8d the electrical conductivity of $La_{1-x}Ba_xCo_{0.8}Nb_{0.2}O_{3-\delta}$ with $0.7 \le x \le 1.0$ exhibits similar behavior. The variation of the electrical conductivity with the chemical composition can be explained considering the defect chemistry of the samples. Using the Kröger-Vink notation and considering $LaCoO_3$ as the undoped stoichiometric reference

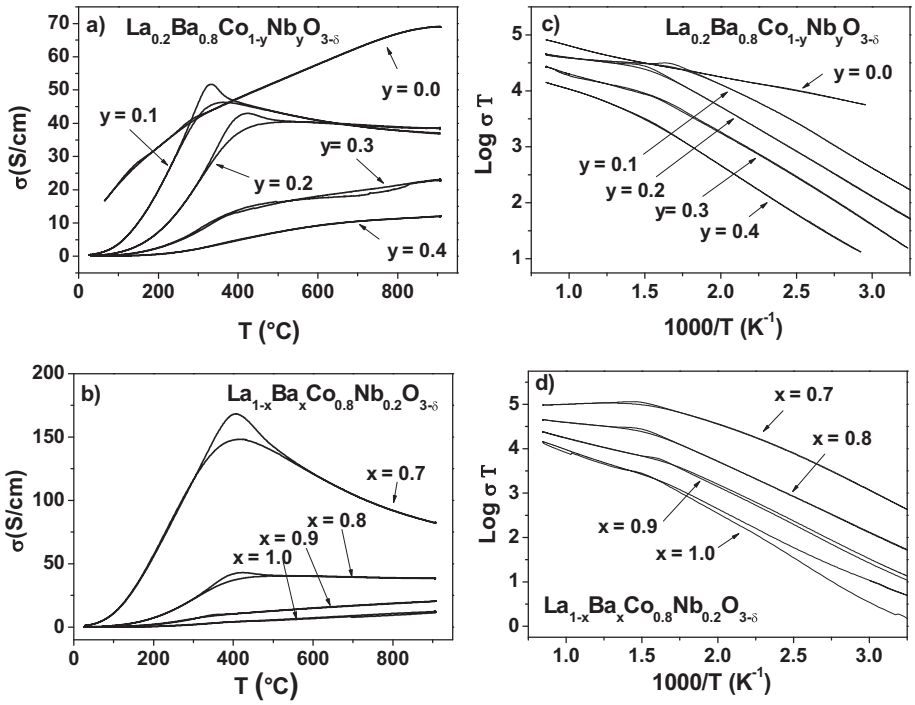

Fig. 8. Electrical conductivity (σ) as a function of temperature for the system $La_{1-x}Ba_xCo_{1-y}Nb_yO_{3-\delta}$. Fig. 8a and b show the plots σ vs. T for $La_{0.2}Ba_{0.8}Co_{1-y}Nb_yO_{3-\delta}$ ($0 \le y \le 0.4$) and $La_{1-x}Ba_xCo_{0.8}Nb_{0.2}O_{3-\delta}$ ($0.7 \le x \le 1.0$), respectively. Fig. 8c and d show the Arrhenius plot, $\log(\sigma T)$ vs $1/T$, for $La_{0.2}Ba_{0.8}Co_{1-y}Nb_yO_{3-\delta}$ ($0 \le y \le 0.4$) and $La_{1-x}Ba_xCo_{0.8}Nb_{0.2}O_{3-\delta}$ ($0.7 \le x \le 1.0$), respectively.

compound, the replacement of La^{3+} by Ba^{2+} is expressed by the incorporation reaction,

$$BaCoO_3 \xrightarrow{LaCoO_3} Ba'_{La} + Co^{\bullet}_{Co} + 3O^{x}_{O} \quad (2)$$

where Ba'_{La}represents a Ba^{2+} cation occupying a La^{3+} crystal site with a negative effective charge, O^{x}_{O} is a regular oxygen lattice ion and $Co^{\bullet}_{Co}$ represents Co^{4+}, which have one effective positive charge. The incorporation of Nb^{5+} in the B site, assuming the presence of $Co^{\bullet}_{Co}$ can be described by the reaction,

$$La_2O_3 + Nb_2O_5 + 4Co^{\bullet}_{Co} \xrightarrow{(La,Ba)CoO_3} 2La^{x}_{La} + 2Nb^{\bullet\bullet}_{Co} + 4Co^{x}_{Co} + 6O^{x}_{O} + O_2 \quad (3)$$

At the same time, the oxygen exchange between the sample and the gas phase, assuming localized electronic defects at $Co^{\bullet}_{Co}$, can be written,

$$O^{x}_{O} + 2Co^{\bullet}_{Co} \leftrightarrow V_O^{\bullet\bullet} + 2Co^{x}_{Co} + 1/2\,O_2 \uparrow \quad (4)$$

where $V^{\bullet\bullet}_{O}$ is a double positive charged oxygen vacancy and Co^{x}_{Co} denotes Co^{3+}. The equilibrium constant for reaction (4) results,

$$K = \frac{[V^{\bullet\bullet}_{O}]\,[Co^{x}_{Co}]^2\,pO_2^{1/2}}{[O^{x}_{O}]\,[Co^{\bullet}_{Co}]^2} \quad (5)$$

From Eqs. (2), (3) and (4) the charge neutrality equation results,

$$[Ba'_{La}] = [Co^{\bullet}_{Co}] + 2\,[V_O^{\bullet\bullet}] + 2[Nb^{\bullet\bullet}_{Co}] \quad (6)$$

As the temperature rises above 350–400 °C, oxygen atoms begin to be removed from the crystal structure increasing the oxygen vacancy concentration and reducing the localized electron holes, according to Eq. (4). This behavior reduces the electronic conductivity [26,27] causing either a maximum or a kink in the σ vs T plots depending on the Nb and Ba contents. If the Nb content is fixed and the Ba content of the samples increases, the neutrality charge Eq. (6) indicates that $[V_O^{\bullet\bullet}]$ and $[Co^{\bullet}_{Co}]$should also increase. In this case, the decrease of the electrical conductivity suggest the oxygen vacancy formation predominates over the formation of $Co^{\bullet}_{Co}$, affecting the electron holes conduction pathways –O–B–O–B–O– of the cubic perovskite and, therefore, the electrical conductivity values [27]. As we described above, the oxygen nonstoichiometry at low temperatures increases with the Ba content, however the variation of the oxygen content with temperature diminishes, as it is revealed by the chemical expansion behavior in Fig. 6, which explains why σ exhibits a maximum for samples with x = 0.7–0.8 or a kink for samples with x = 0.9–1.0. Similar behavior was reported for $Ba_xSr_{1-x}Co_{0.8}Fe_{0.2}O_{3-\delta}$ [9] and $Ba_xSr_{1-x}Co_yFe_{1-y}O_{3-\delta}$ [27]. On the other hand, if the Ba content is fixed and the Nb content increases, Eq. (6) indicates that$[V_O^{\bullet\bullet}]$and $[Co^{\bullet}_{Co}]$ should decrease and thereby also should the amplitude of the oxygen nonstoichiometry above 350 °C–400 °C. Thus, in this case, the presence of Nb affects the –O–B–O–B–O– pathways reducing σ, while the lower variation of the oxygen nonstoichiometry with temperature is responsible of the slope change of the log (σ) vs. T data above 350 °C–400 °C (Fig. 8a) as the Nb content increases.

3.4. Oxygen permeation

In Fig. 9a-c we show the variations of the oxygen permeation flux (jO_2) as a function of the oxygen partial pressure gradient (log pO_2'/pO_2'') for ceramic membranes of $La_{1-x}Ba_xCo_{0.8}Nb_{0.2}O_{3-\delta}$ with $0.7 \le x \le 0.9$ at 700 °C, 800 °C and 930 °C. Measurements were performed on membranes 1.0 mm thick. The oxygen permeation flux increases as ΔpO_2 across the membrane or the temperature increases. Fig. 10 shows the variation of jO_2 with temperature at fixed log(pO_2'/pO_2'') = 0.75 for the series $La_{0.2}Ba_{0.8}Co_{1-y}Nb_yO_{3-\delta}$ with

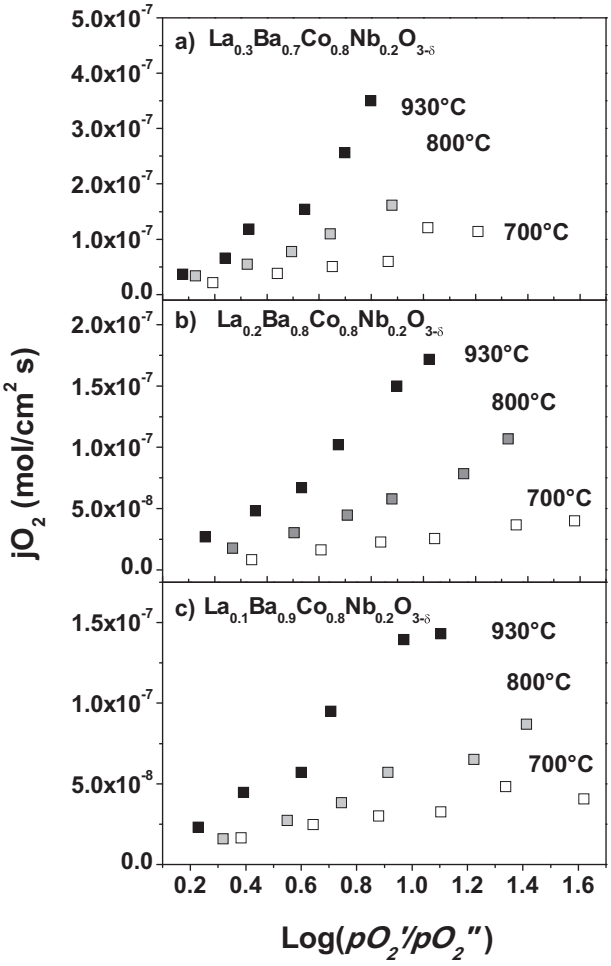

Fig. 9. Variation of jO_2 with log (pO_2'/pO_2'') at various temperatures for ceramic membranes of $La_{1-x}Ba_xCo_{0.8}Nb_{0.2}O_{3-\delta}$ ($0.7 \le x \le 0.9$). a) x = 0.7, b) x = 0.8 and c) x = 0.9.

$0.1 \le y \le 0.4$ and $La_{1-x}Ba_xCo_{1-y}Nb_yO_{3-\delta}$ with $0.7 \le x \le 0.9$ in an Arrhenius plot. Clearly, for a fixed Ba content, x = 0.8, the incorporation of Nb^{5+} replacing Co^{3+} lowers the oxygen permeation flux values, in agreement with experimental data reported by Fang et al. [14] for Nb-substituted $Ba_{0.5}Sr_{0.5}Co_{0.8}Fe_{0.2}O_{3-\delta}$ membranes. This behavior

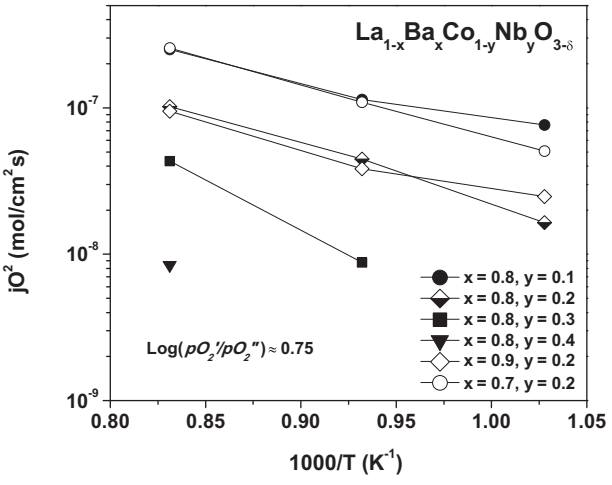

Fig. 10. Arrhenius plot of the variations of the oxygen permeation flux (jO_2) for $La_{1-x}Ba_xCo_{1-y}Nb_yO_{3-\delta}$ at log (pO_2'/pO_2'') = 0.75.

Table 2
Oxide ion conductivity, $\overline{\sigma}_i$, calculated from oxygen permeation data, total conductivity, σ_T, determined from electrical conductivity and ionic transport number $t = \overline{\sigma}_i/\sigma_T$.

	$\overline{\sigma}_i$ (S cm^{-1}) 700 °C	σ_T (S cm^{-1})	$\overline{\sigma}_i/\sigma_T$ ($^{3}_{\times 10}$)	$\overline{\sigma}_i$ (S cm^{-1}) 800 °C	σ_T (S cm^{-1})	$\overline{\sigma}_i/\sigma_T$ ($^{3}_{\times 10}$)	$\overline{\sigma}_i$ (S cm^{-1}) 930 °C	σ_T (S cm^{-1})	$\overline{\sigma}_i/\sigma_T$ ($^{3}_{\times 10}$)
$La_{0.2}Ba_{0.8}Co_{0.9}Nb_{0.1}O_{3-\delta}$	0.08	39.1	2	0.14	38	3.7	0.23	37	6.2
$La_{0.2}Ba_{0.8}Co_{0.8}Nb_{0.2}O_{3-\delta}$	0.02	39.6	0.5	0.05	39	1.3	0.10	38	2.7
$La_{0.2}Ba_{0.8}Co_{0.9}Nb_{0.3}O_{3-\delta}$	–	–	–	0.005	21.4	0.25	0.025	23	1.1
$La_{0.1}Ba_{0.9}Co_{0.8}Nb_{0.2}O_{3-\delta}$	0.025	16.7	1.5	0.04	18.5	2.15	0.085	21.5	3.9
$La_{0.3}Ba_{0.7}Co_{0.8}Nb_{0.2}O_{3-\delta}$	0.075	105	0.7	0.13	92	1.4	0.22	81	2.7

correlates with the reduction of the oxygen vacancy concentration for $La_{0.2}Ba_{0.8}Co_{1-y}Nb_yO_{3-\delta}$ as the Nb content increases, as described in the previous section. On the other hand, for samples with fixed Nb content at y = 0.2, the jO_2 values obtained for the sample with x = 0.7 were higher than those obtained for samples with x = 0.8 and 0.9. This result deviates from the fact that the oxygen vacancy concentration increases with the Ba content and therefore higher jO_2 values would be expected. Assuming the oxygen transport across the membranes in this system is limited by the oxide ion diffusion in the bulk, jO_2 can be describe with the Wagner's equation [2],

$$jO_2 = -\frac{RT}{16F^2L}\int_{\ln(pO_2')}^{\ln(pO_2'')}\frac{\sigma_e\sigma_i}{\sigma_i+\sigma_e}d\ \ln(pO_2) \tag{7}$$

where R is the gas constant, F is the Faraday constant, T is the temperature, L is the thickness of the membrane, and σ_e and σ_i are the electronic and ionic conductivity, respectively. Because the electrical conductivity of these materials at $T \geq 500$ °C is larger than 10 S cm^{-1} (see Fig. 8), it is reasonable to assume that the oxygen permeation flux is controlled by their ionic conductivity [2,25,26]. Thus, Eq. (7) can be simplified as

$$jO_2 = \frac{RT}{16F^2L}\overline{\sigma}_i\ \ln\left(pO_2'/pO_2''\right) \tag{8}$$

where $\overline{\sigma}_i$ is the average oxide ion conductivity at constant T, in the pO_2 range of the experimental data, and can be computed from the slope of the jO_2 vs. $\ln(pO_2'/pO_2'')$ curves. In Table 2 the oxide ion conductivity values, $\overline{\sigma}_i$, calculated from oxygen permeation data at T = 700, 800 and 930 °C, the total conductivity, σ_T, determined from electrical conductivity data (Section 3.3), and the ionic transport number, $t = \overline{\sigma}_i/\sigma_T$, are listed. The oxide ion conductivity values are comparable to those previously published for perovskites with Co in the B site [24,26]. Clearly, the diminution of jO_2 with either increasing Nb or Ba content is reproduced by the oxide ion conductivity values listed in Table 2.

3.5. Impedance measurements

The polarization resistances of $La_{1-x}Ba_xCo_{1-y}Nb_yO_{3-\delta}$ electrodes have been determined by impedance spectroscopy measurements using symmetrical cells in the temperature range 450 °C ≤ T ≤ 850 °C, in air. Fig. 11 shows a SEM micrograph of the electrode cross-section of a cell prepared with $La_{0.2}Ba_{0.8}Co_{0.9}Nb_{0.1}O_{3-\delta}$. Good connectivity between the electrode and the electrolyte was observed for all the cells. Impedance spectra were found to be similar to those obtained for the system $La_{1-x}Ba_xCo_{1-y}Fe_yO_{3-\delta}$ [6]. Thus, impedance data were fitted using an equivalent circuit consisting of a resistor, representing the ohmic resistance of the electrolyte, in series with an inductance, representing the cables of the experimental setup, and elements (Ri,CPE) in series [6]. At $T \geq 600$ °C only two elements (Ri,CPE) were needed to reproduce two impedance arcs at intermediate (IF) and low frequency (LF) ranges with characteristic values 300 ≤ ν_{IF} ≤ 900 Hz and 1 ≤ ν_{LF} ≤ 2.3 Hz, respectively. Only for the $La_{0.2}Ba_{0.8}Co_{0.6}Nb_{0.4}O_{3-\delta}$ electrode the LF contribution was not detected and two contributions with characteristic frequency in the intermediate range were used. Fig. 12 shows the impedance spectra at constant temperature, T = 600 °C, for electrodes with fixed Ba content, x = 0.8, and Nb content varying from y = 0.1 to y = 0.4. Clearly, the intermediate frequency contribution is affected by the chemical composition of the electrode, in this case the Nb content. The total polarization resistance values (Rp) were obtained by adding the ohmic contributions of the (Ri,CPE) elements. Fig.13a and b show the variation of Rp with the Ba and Nb contents at T = 600 °C for $La_{0.2}Ba_{0.8}Co_{1-y}Nb_yO_{3-\delta}$ with 0.1 ≤ y ≤ 0.4 and $La_{1-x}Ba_xCo_{0.8}Nb_{0.2}O_{3-\delta}$ with 0.7 ≤ x ≤ 1.0, respectively. Fig. 13a clearly shows that Rp increases with the Nb content of the electrode, thus the highest value Rp = 6.5 Ω cm^2 corresponds to the

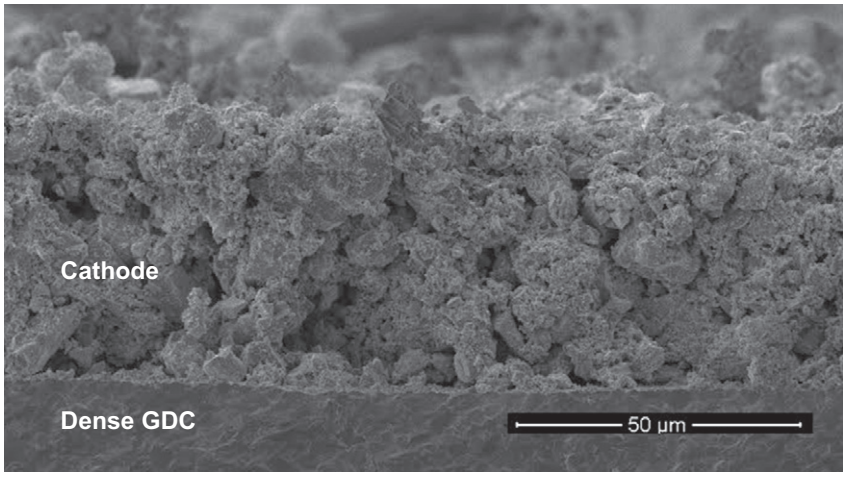

Fig. 11. SEM micrograph of the electrode cross-section prepared with $La_{0.2}Ba_{0.8}Co_{0.9}Nb_{0.1}O_{3-\delta}$.

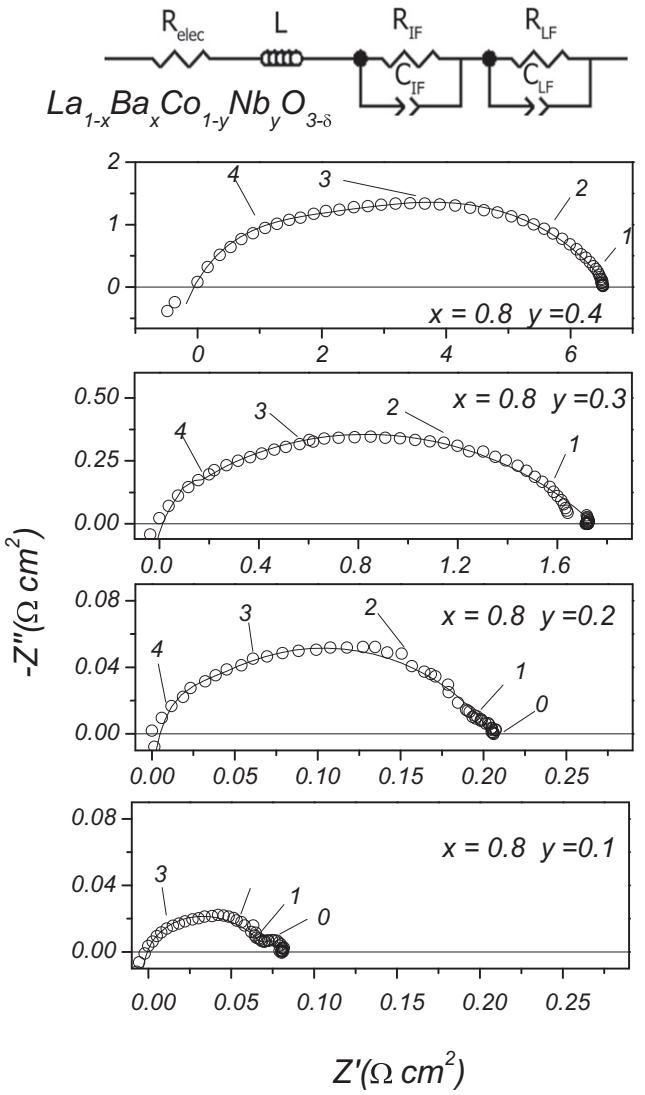

Fig. 12. Complex impedance spectra of $La_{1-x}Ba_xCo_{1-y}Nb_yO_{3-\delta}$ electrodes at $T = 600$ °C, in air. The solid line corresponds to the fit of the experimental data using the equivalent circuit displayed at the top of the figure. The logarithm of the frequency is indicated in the figures.

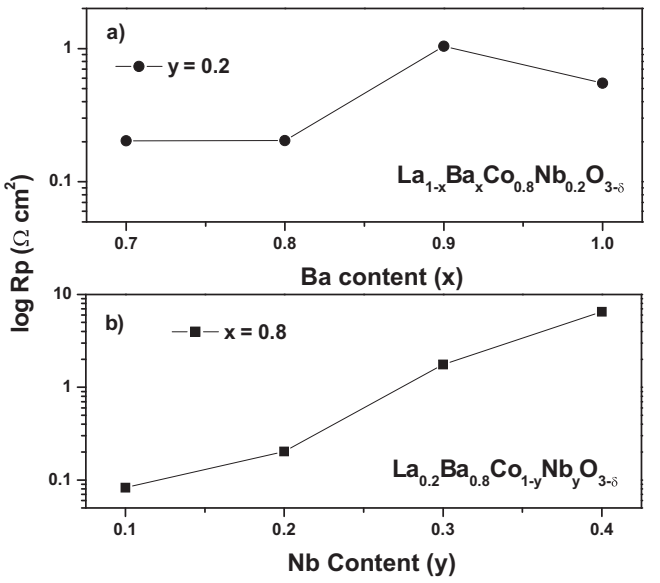

Fig. 13. Variation of the polarization resistance, Rp, for $La_{1-x}Ba_xCo_{1-y}Nb_yO_{3-\delta}$ electrodes with the chemical composition. Variation of Rp with: a) the Ba content and b) the Nb content. Measurements were performed at 600 °C, in air, using symmetrical cells.

sample with y = 0.4, while the minimum value Rp = 0.08 Ω cm^2 was obtained for the electrode with y = 0.1. Similar behavior related to the incorporation of Nb in the perovskite structure was reported for $La_{0.1}Sr_{0.9}Co_{1-y}Nb_yO_{3-\delta}$ with $0.1 \le y \le 0.2$ [28] and $BaCo_{0.3}Fe_{1-y}Nb_yO_{3-\delta}$ with $0.00 \le y \le 0.12$ [15]. On the other hand, those electrodes with fixed Nb content y = 0.2 show the lowest values Rp ~ 0.2 Ω cm^2 for x = 0.7–0.8 (Fig. 13a). The Rp = 0.08 Ω cm^2 value obtained for $La_{0.2}Ba_{0.8}Co_{0.9}Nb_{0.1}O_{3-\delta}$ results slightly higher than those values Rp ~ 0.065–0.075 Ω cm^2 obtained for graded cathodes using $La_{0.4}Ba_{0.6}CoO_{3-\delta}$ [29,30].

4. Conclusions

The solubility of Nb^{5+} in the system $La_{1-x}Ba_xCo_{1-y}Nb_yO_{3-\delta}$ with high Ba content ($0.6 \le x \le 1.0$) and its effects on the high temperature properties have been studied. The solubility of Nb in the cubic perovskite increases from y = 0.1, for Ba content x = 0.6 ,to y = 0.4, for $0.8 \le x \le 1.0$. The incorporation of Nb in the B site stabilizes the cubic perovskite in the as prepared samples. The crystal structure stability was evaluated by heat treating the samples at 750 °C during 10 days. XRD data show the appearance of small amounts of secondary phases for samples with x = 0.9 and 1.0. For x = 0.6, 0.7 and 0.8 we found stable cubic phases for y = 0.1, $0.1 \le y \le 0.3$ and $0.2 \le y \le 0.4$, respectively. The lattice parameter of the cubic cell increases with the Nb content. The linear expansion of the cubic phases decreases with both the Nb and the Ba content due to a reduction of the chemical expansion. The lowest total linear expansion value, 12.9×10^{-6} K^{-1}, for the temperature range $30 \le T \le 900$ °C, was obtained for $La_{0.8}Ba_{0.2}Co_{0.6}Nb_{0.4}O_{3-\delta}$. The incorporation of Nb^{5+} replacing Co^{3+} as well as the incorporation of Ba^{2+} affect the O–B–O–B–O– conduction pathways of the electron holes reducing, in both cases, the electrical conductivity. Oxygen permeation flux and, thereby, the ionic conductivity decrease with the Nb content of the samples. The electrode polarization resistance at 600 °C displays a minimum, Rp = 0.08 Ω cm^2, for $La_{0.2}Ba_{0.8}Co_{0.9}Nb_{0.1}O_{3-\delta}$. The experimental data show that while the increase of Nb content reduces the electrochemical performance of the material as a cathode, it improves the structural stability of the cubic perovskite. Thus, a suitable balance between these two properties make the perovskite system $La_{1-x}Ba_xCo_{1-y}Nb_yO_{3-\delta}$ with $x \ge 0.7$ and $0.1 \le y \le 0.3$ of interest for high temperature electrochemical applications.

Acknowledgment

The authors thank A. Prado for English revision of the manuscript. This work was supported by Comisión Nacional de Energía Atómica (CNEA), Consejo Nacional de Investigaciones Científicas y Técnicas (CONICET) and Agencia Nacional de Promoción Científica y Técnica (ANPCyT), Argentina, through PIP 112 2013 0100151 CO, and PICT 2013-1032 and 2013-1587, respectively.

References

[1] S.B. Adler, Chem. Rev. 104 (2004) 4791.
[2] J. Sunarso, S. Baumann, J.M. Serra, W.A. Meulenberg, S. Liu, Y.S. Lin, J.C. Diniz da Costa, J. Membr. Sci. 320 (2008) 13.
[3] Y. Teraoka, H.M. Zhang, S. Furukawa, N. Yamazoe, Chem. Lett. 1743 (1985).
[4] T. Ishihara, S. Fukui, H. Nishiguchi, Y. Takita, J. Electrochem. Soc. 149 (2002), A823. .
[5] C. Setevich, L. Mogni, A. Caneiro, F. Prado, J. Electrochem. Soc. 159 (2012), B73. .
[6] C. Setevich, D.Z. de Florio, A. Caneiro, F. Prado, J. Power Sources 247 (2014) 264.
[7] C. Chanquía, L. Mogni, H. Troiani, A. Caneiro, J. Power Sources 270 (2014) 457.
[8] S. Haile, Z. Shao, Nature 431 (2004) 170.
[9] H. Prata, S.K. Rout, S.K. Pratihar, S. Bhattacharya, Int. J. Hydrog. Energy 36 (2011) 11904.
[10] G.M. Rupp, A. Schmid, A. Nenning, J. Fleig, J. Electrochem. Soc. 163 (2016), F564. .

[11] S. Švarcová, K. Wiik, J. Tolchard, H.J.M. Bouwmeester, Tor Grande, Solid State Ionics 178 (2008) 1787.
[12] M. Arnold, T. Gesing, J. Martynczuk, A. Feldhoff, Chem. Mater. 20 (2008) 5851.
[13] T. Nagai, W. Ito, T. Sakon, Solid State Ionics 177 (2007) 3433.
[14] S.M. Fang, C.–.Y. Yoo, H.J.M. Bouwmeester, Solid State Ionics 195 (2011) 1.
[15] M. Harada, K. Domen, M. Hara, M. Tatsumi, Chem. Lett. 35 (2006) 968.
[16] C. Zhu, X. Liu, C. Yi, L. Pei, D. Yan, J. Niu, D. Wang, W. Su, Electrochem. Commun. 11 (2009) 958.
[17] J. Rodríguez-Carvajal. Fullprof: A Program for Rietveld Refinement and Profile Matching Analysis of Complex Powder Diffraction Patterns, Laboratoire Léon Brillouin (CEA-CNRS).
[18] Zview version 2.0b copyright 1990–2005, Scribner Associates, Inc. D. Johnson.
[19] A.J. Jacobson, J.L. Hutchison, J. Solid State Chem. 35 (1980) 334.
[20] K. Yamaura, R. Cava, Solid State Commun. 115 (2000) 301.
[21] R. Shannon, Acta Crystallogr. Sect. A 32 (1976) 751.
[22] S. Adler, J. Am. Ceram. Soc. 84 (2001) 2117.
[23] X. Chen, J. Yu, S.B. Adler, SB, Chem. Mater. 17 (2005) 4537.
[24] Y. Teraoka, H.M. Zhang, K. Okamoto, N. Yamazoe, Mat, Res. Bull. 23 (1988) 51.
[25] J.-H. Kim, L. Mogni, F. Prado, A. Caneiro, J.A. Alonso, A. Manthiram, J. Electrochem. Soc. 156 (2009), B1376. .
[26] J.W. Stevenson, T.R. Armstrong, R.D. Carneim, L.R. Pederson, W.J. Weber, J. Electrochem. Soc. 143 (1996) 2722.
[27] Z. Yáng, A.S. Harvey, A. Infortuna, J. Schoonman, L. Gauckler, J. Solid State Electrochem. 15 (2011) 277.
[28] S. Yoo, J. Kim, S. Song, D. Lee, J. Shin, K. Ok, G. Kim, RSC Adv. 4 (2014) 18710.
[29] C. Setevich, L. Mogni, A. Caneiro, F. Prado, Int. J. Hydrog. Energy 37 (2012) 14895.
[30] C. Setevich, F. Prado, D.Z. de Florio, Int. J. Hydrog. Energy 39 (2014) 8738.